Vacuum 110 (2014) 114–120

Contents lists available at ScienceDirect

Vacuum

journal homepage: www.elsevier.com/locate/vacuum

Structural peculiarities and aging effect in hydrogenated a-Si prepared by inductively coupled plasma assisted chemical vapor deposition technique

G. Nogay [a, b, *], E. Özkol [b, c], S. Ilday [b], R. Turan [a, b]

[a] Department of Physics, Middle East Technical University (METU), 06800 Ankara, Turkey
[b] Center of Solar Energy Research and Application (GÜNAM), Middle East Technical University (METU), 06800 Ankara, Turkey
[c] Department of Chemical Engineering, Middle East Technical University (METU), 06800 Ankara, Turkey

ARTICLE INFO

Article history:
Received 2 May 2014
Received in revised form
8 September 2014
Accepted 10 September 2014
Available online 18 September 2014

Keywords:
Inductively coupled plasma assisted PECVD
Ballistic growth
Aging effect
Oxidation
Cauliflower-like Si nanostructure

ABSTRACT

In this study, we report the morphological and structural properties of amorphous and nanocrystalline Si thin films deposited by inductively coupled plasma-assisted chemical vapor deposition (ICP-CVD) technique at low substrate temperatures using H_2 diluted SiH_4 as the source gas. We demonstrated that changing the total deposition pressure across a broad range alters the film properties. The film grew in a columnar fashion, and its topography was rough at nanoscale as identified by high resolution Transmission Electron Microscopy (TEM), independent of its amorphous or crystalline nature. Further investigation of the structure revealed that the columns consisted of structures resembling highly porous cauliflower. Additionally, these cauliflower-like Si nanostructures oxidized gradually and extremely uniform throughout the film when exposed to air due to their highly porous nature. We have explained the formation of these structural properties using ballistic growth theory and reactive radicals' effect.

1. Introduction

Hydrogenated amorphous (a-Si) and nano/micro-crystalline silicon (nc-/μc-Si) thin films are major materials for today's Si-based thin film solar cell technology. They permit large area deposition at relatively low temperature with low base material usage (a few μm) and less process steps whereas crystalline Si (c-Si)-based solar cell technology requires delicate wafer preparation with numerous process steps [1–3]. They have low energy pay-back time and can be deposited on cheaper substrates such as glass, plastic foil, stainless steel, etc. [4]. However, limited cell efficiencies remain the major disadvantage of a/nc/μc-Si thin films-compared with c-Si-based solar cells [5]. Materialistic constraints such as light-induced degradation cause a significant efficiency drop in a-Si thin film solar cells [6]. In contrast, nc/μc-Si thin films suffer less from light-induced degradation and offer a tunable band gap with the possibility of fabricating tandem solar cells. In recent optimization studies, stable sub-module efficiencies of a-Si and nc/μc-Si thin film tandem solar cells have exceeded 11.7% [7].

Si thin films with sufficiently good quality are commonly fabricated by plasma enhanced chemical vapor deposition (PECVD) with a capacitively coupled plasma (CCP) configuration [8]. However, this technique has some drawbacks, especially for nc-Si thin film deposition, because it requires high deposition pressures and powers, which result in powder formation, delamination of the film due to accumulated stress on surface and directional high-energy ion bombardment of the film [9,10]. Based on the critical role of H_2 in nucleation [11], nc-Si thin films are deposited only when SiH_4 is heavily diluted with H_2, which leads to a decrease in the deposition rate and an increase in gas and power consumption [12]. To overcome these drawbacks, high-density plasma sources such as an inductively coupled plasma (ICP) source, which is a rich ion and radical source, are recommended. ICP provides higher deposition rates owing to its higher dissociation capacity and low plasma sheath potential that reduces the ion bombardment. The high dissociation capacity also leads to crystallization at low temperatures, which is very important for applications on thermo-sensitive flexible substrates [13]. Finally, uniformity of the plasma in the radial and axial directions provides a good spatial homogeneity in the deposited film [14].

* Corresponding author. École Polytechnique Fédérale de Lausanne EPFL STI IMT PV-LAB Microcity, Rue de la Maladière 71B, CH-2000 Neuchatel, Switzerland. Tel.: +41 021 695 43 08; fax: +41 021 695 42 01.
E-mail address: gizem.nogay@epfl.ch (G. Nogay).

http://dx.doi.org/10.1016/j.vacuum.2014.09.006
0042-207X/

Recently, a number of promising applications of ICP-CVD have been reported. A good example is the effective surface passivation of c-Si using an intrinsic Si layer deposited by an ICP source [15,16]. Research has indicated that the excellent uniformity along the growth direction could minimize the incubation layer between passivation layer and substrate for hetero-junction solar cell applications. Furthermore, relatively high conversion efficiencies have been obtained without any back-surface field or texturing [17]. Apart from a-Si:H films, ICP-CVD-deposited SiN_x:H thin films have also exhibited excellent passivation and an anti-reflection effect on p- and n-type Si substrates; this has been confirmed by the improved performance of c-Si solar cells [18]. Fundamental properties of ICP-CVD-deposited SiN_x:H films has been published recently to show that it is also possible to use this technique for MEMS applications [19]. As an example of a conventional thin film solar cell, single junction a-Si:H solar cells with a conversion efficiency of 9.6% have been realized using ICP-CVD [20]. An ICP-CVD system has been used in third generation solar cell applications; the system utilizes optical band-gap tuning of ultrathin multilayers that allow Si tandem solar cells [21]. This system exhibited improved light-soaking stability thanks to the high degree of crystallinity and thus stability in the chemical structure of the film [20]. Within this context, the ICP silane plasma has been shown to be an effective tool for semiconductor nanoparticle fabrication, yielding extremely mono-disperse, discrete, spherical, and size-controllable nanoparticles [22].

In this study, we describe the structural peculiarities observed in a-Si and nc-Si thin films fabricated by ICP-CVD and the effect of aging on the chemical properties of these materials. In agreement with previous reports, crystal formation was possible even at low temperatures [23] just by changing the deposition pressure. The films grew in a columnar fashion with a high porosity and a fairly rough surface topology. These columnar structures appeared to be independent of the amorphous and crystalline nature of the films. Further investigation of the structure revealed that the columns consist of structures resembling cauliflower. Here, we discuss the formation of this remarkable film structure in terms of two approaches based on plasma properties and deposition kinetics [24]. We have identified structural similarities with different other materials and discuss this formation in terms of so-called ballistic growth mechanism. Furthermore, it is showed that these cauliflower-like Si nanostructures oxidize gradually and uniformly throughout the film when exposed to air due to their highly porous nature and continue to do so for up to several days' weeks. We believe that this effect is responsible for the large band gap and poor electrical properties associated with these films.

2. Experimental details

500 nm thick a-Si:H and nc-Si:H thin films were fabricated using diluted SiH4 (10% in H2) at room temperature by ICP-CVD onto p-type (100) Si-wafer with a resistivity of 10–20 Ω-cm and Corning Eagle-XG glass substrates. Although the depositions had been performed at room temperature, the substrate temperature was higher than the room temperature due to radiative heating and a high flux of energetic ion bombardment during the process [25]. At room temperature, substrate temperature was measured as 20 °C before the process from the back side of the substrate. During the process, it has been observed that substrate temperature is increasing slowly with time. At the beginning of process it was 38 °C and after 15 min, at the end of the process, it was defined as 120 °C.The inductive source was operated at a radio frequency (RF) of 13.56 MHz. The total deposition pressure was varied to control the structure and morphology. During deposition, the SiH_4 flow and power density were held constant at 9 sccm and 0.16 W/cm^3, respectively. The morphology of the samples was identified by high-resolution transmission electron microscopy (HR-TEM) (JEOL-JEM 2100F operated at 200 kV) and high-resolution field emission scanning electron microscopy (SEM: FEI QUANTA 400F operated at 10 kV). For TEM specimen preparation, films were scratched out from the substrate gently into the ethanol; ethanolic solution was drop casted onto lacey carbon coated copper grids and allowed to dry in atmosphere. The structural analyses were conducted via Raman spectroscopy (RS) (Horiba-Jobin Yvon i550 system equipped with a 532 nm laser), and grazing incidence X-ray diffraction spectroscopy (GI-XRD) (Rigaku Ultima IV, incidence line of CuK_α with a wavelength of 1.540562 Å and fixed incidence angle of 0.3°). The chemical composition was identified using X-ray photoelectron spectroscopy (XPS) (PHI 5000 Versa Probe with monochromatic Al K_α excitation as the X-ray source with the power of 22.1W), with Ar ion etching used for depth profiling studies. XPS measurements were performed with 100 μm spot size, 45^0 take off angle and 58.7 eV pass energy. Ar-ion gun was operated at the beam energy of 2 keV for 2 mm × 2 mm sputter area with 0.2 eV energy steps, 200 ms dwell time, 4 sweeps. We have analyzed the data using the program Multipak Software Version 9.5 which assumes the same RSF value for each profile taken during the depth profiling. For the hydrocarbon effect, we used C 1s peak obtained from the very top layer of the film to make correction for the charging effect. The C peak disappeared after removal of the top surface layers. We have, however, observed that peak positions did not vary in all layers we analyzed, so that, we can assume that initial calibration remain valid during the depth profiling procedures. Fourier-transform infrared spectroscopy (FTIR) (Brucker Equinox 55 IR Spectrometer in the mid-infrared range from 400 to 4000 cm^{-1}) was also performed to identify the chemical bonding configuration and aging effect.

3. Results and discussion

3.1. Plasma diagnostics and deposition rate

Before discussing the film properties, we believe it is important to discuss general plasma properties as studied by optical emission spectroscopy (OES) so that the glow discharge mechanisms during the deposition of a- and nc-Si and the influence of deposition conditions on plasma properties are understood. Fig. 1(a) shows the results of OES of highly H_2-diluted SiH_4 plasma as a function of the deposition pressure; the thin vertical dotted lines specify the positions of commonly used emission lines for plasma analyses. H^*_α, H^*_β, and SiH^* species can be detected in an OES spectrum with emission signals located at 656 nm, 485 nm, and 412 nm, respectively [26]. Fig. 1(b) shows the intensity of signals originated from these species. In general, the deposition rate increased with deposition pressure in correlation with an increased amount of reactive radicals such as SiH^*, H^*_α, and H^*_β. When the deposition pressure was increased, the numbers of molecules inside the vacuum chamber at a constant silane gas flow also increased because there were more SiH_4 molecules to dissociate into reactive radicals.

It is well known that ICP provides sources of favorable reactive species, leading to a high deposition rate. The variation of the deposition rate as a function of deposition pressure is presented in Fig. 1(c). Deposition rates as high as 65 nm/min were reached at high deposition pressures; high deposition rates are desirable for the deposition of thick nc-/μc-Si layers in tandem solar cells. The observed deposition rates in this study were significantly higher than those obtained with a conventional PECVD system equipped with an RF source. Only a very high frequency PECVD system is able to achieve similar deposition rates [27,28].

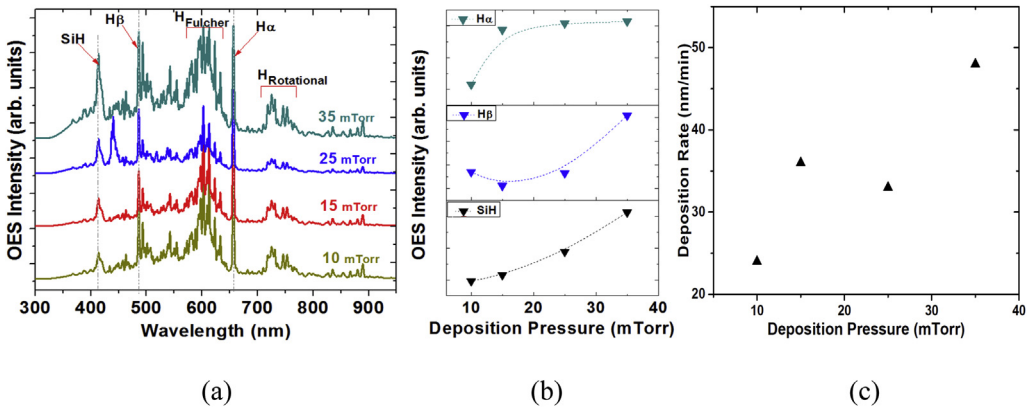

Fig. 1. (a) The effect of deposition pressure on optical emission spectroscopy (OES) spectra of the thin films, (b) OES intensity change as a function of the deposition pressure of detectable plasma species, (c) Variations in deposition rate as a function of the deposition pressure.

The SiH signal located at 414 nm is a measure of the silane depletion rate [29]; the depletion rate increases as the intensity of this peak diminishes. In agreement with previous observations [29], we found that the transition from the amorphous to microcrystalline phase occurred when the SiH peak decreased, which means that crystallinity is strongly affected by silane depletion. In this study, the highest crystallinity was observed at the lowest deposition pressure, which is associated with the highest silane depletion rate. The additional peak seen at around 440 cm^{-1} in the sample produced with 25 mTorr is not related to SiH at all. It is originated from SiN, which is typically observed at the beginning of the deposition process probably due to N element coming from the chamber cleaned with NF_3 prior to the deposition [30].

3.2. Surface morphology and cauliflower-like columnar growth

Surface topography and cross-sectional SEM images of nc-Si (Fig. 2(a) and (b)) and a-Si (Fig. 2(d) and (e)) thin films and their crystallinities (Fig. 2(c) and (f)), analyzed via RS, are shown in Fig. 2. It is clear from the cross-sectional images that both nc- and a-Si thin films grew in a columnar fashion.

In previous studies, the columnar growth of ICP-CVD-deposited a- and nc-Si thin films has been explained by the domination of certain reactive plasma species, specifically SiH_x ($0 \leq x \leq 2$). It is well known that ICP-CVD systems can produce high-density plasmas, which have a high dissociation capacity of SiH_4 and H_2 due to inelastic interactions with electrons. Following the dissociation of silane, reactive species such as Si^*, SiH^*, SiH_2^*, SiH_3^*, and H_2 are produced. Generally, SiH_3 radicals are considered the main contributor to thin film formation due to their low reactivity and long lifetime [31,32]. SiH_3 radicals have high surface diffusion; therefore, they generally find the most suitable place before reacting with other species. In contrast, any SiH_x ($0 \leq x \leq 2$) species arriving at an a-Si:H surface has difficulty sticking; they are highly reactive and have short lifetimes. These radicals can react immediately even at room temperature. The dominance of SiH_x ($0 \leq x \leq 2$) species in plasma under certain conditions can result in a columnar microstructural growth due to the limited lateral diffusion [33,34], as was observed in our study. Even so, this model is not sufficient to fully explain the observed columnar growth.

We believe that a more convincing explanation can be achieved using the well-known ballistic growth theory [24,35]. According to

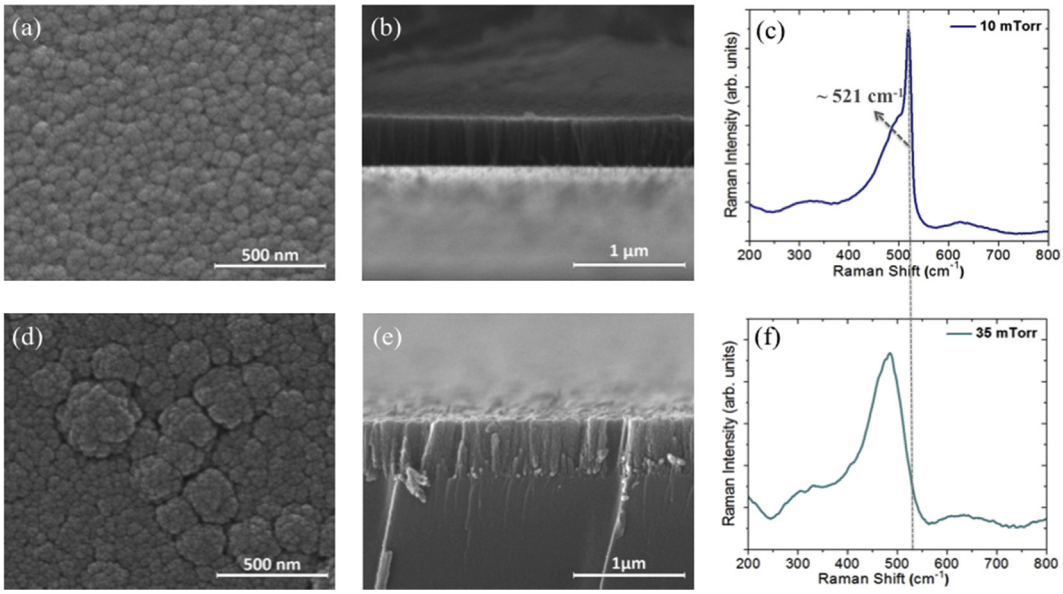

Fig. 2. (a) Surface topography and (b) Cross-sectional SEM images of nc-Si thin film, (c) RS spectra of nc-Si thin film. (d) Surface topography and (e) Cross-sectional SEM images of a-Si thin film, (f) RS spectra of a-Si thin film.

this theory, particles colliding on a substrate via a straight vertical trajectory from a random position will stick to the substrate [36–38]. During the deposition, no heat is applied to the substrate, which restricts the surface diffusion of the incoming particles. Restricted lateral diffusion eventually forces the structure to grow vertically; hence, the columnar growth. A detailed mathematical description of ballistic growth theory can be found in references 20 and 30. This simple method provides control over the film morphology, porosity and directional growth. In short, columnar growth via the ballistic deposition is independent of the material type; it is purely related to the deposition kinetics. In this study, investigation of the surface topologies of the films showed that the structure closely resembles cauliflower. In a recent study on WO_3, cauliflower-type growth has also been observed and successfully described by the ballistic growth model [39]. The visible structural similarities between quite different materials including WO_3 [39], TO_2 [40], MgO [41] and a-Si/nc-Si are surprising.

To further understand the inner structure of these cauliflower-like structures, we performed HRTEM imaging analyses. The structure was organized in a dendritic form with a high degree of porosity (Fig. 3(a)). The individual wire-like structures are bundled together during the deposition until a critical radius is formed (Fig. 3(b)). When these bundles form next to each other, they begin forming these cauliflower-like structures on the surface of thin films. In the ballistic growth, the lateral diffusion is restricted, but a small number of atoms/clusters are moved to the next unoccupied site on the surface instead of sitting on top of an already occupied site. This leads to an angular lateral expansion of the bundles, which results in the formation of dendritic structures. This formation makes a large contribution to the porosity, which is the main reason for the aging affect we discuss below. Recently, theoretical studies by Robledo et al. [35] and Saito et al. [37] have described the formation of these dendritic structures extensively by modeling the dynamics of angular expansion during columnar growth using deposition theory; these studies are consistent with our experimental findings. Although these structures and non-uniformity may be considered poor film quality, the columnar structures provide effective channels for vertical carrier transport when applied to solar cells [42]. This structure also offers a new way of fabricating columnar nanostructures, giving rise to the quantum size effect that can be utilized in third generation solar cells. Formation kinetics and optical properties of the nanocrystal formed by this technique will be discussed in a separate report.

3.3. Crystallinity

RS and XRD measurements were performed to estimate the crystal volume fraction of the a- and nc-Si thin films. Fig. 2(c) and (f) show the RS spectra of two samples prepared at different deposition pressures. It is well recognized that the Si:H RS signal is comprised of three phases: the amorphous phase (~480 cm^{-1}); intermediate phase (~510 cm^{-1}), originating from the defective part of crystalline phase associated with grain boundaries [43]; and crystalline phase (~521 cm^{-1}), related to the transverse optical (TO) mode of Si–Si vibrations [44]. The crystal volume fraction of Si-thin films can be determined by the integrated area ratio:

$$X_c = \frac{I_c + I_i}{(\alpha I_a + I_c + I_i)} \quad (1)$$

where I_a,I_i, and I_c are the integrated area of amorphous, intermediate, and crystalline phases RS signals, respectively. The factor α is estimated as 1 because the crystal diameters are very small [42,45]. It is also obvious from Fig. 2 that the c-Si signal becomes prominent as the deposition pressure was reduced, which suggests that the crystalline phase becomes dominant due to enhanced crystallization.

When the deposition pressure was above 25 mTorr, the film remained in the amorphous phase; when the pressure was below 25 mTorr, the film transitioned from a-Si:H to nc-Si, as indicated by the emergence of a narrow peak at 521 cm^{-1}. The intensity of the crystal signal increased as the deposition pressure decreased. The maximum Raman crystallinity (X_C) was 49% for thin films prepared at 10 mTorr deposition pressure and it is decreasing with increasing deposition pressure values (see Table 1).

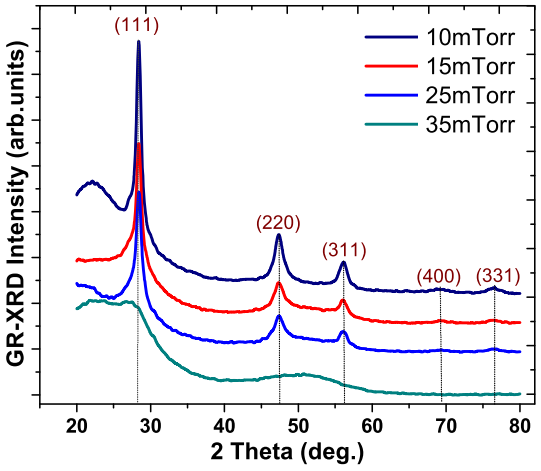

Fig. 4. GI-XRD spectra of the Si thin films deposited at various deposition pressures.

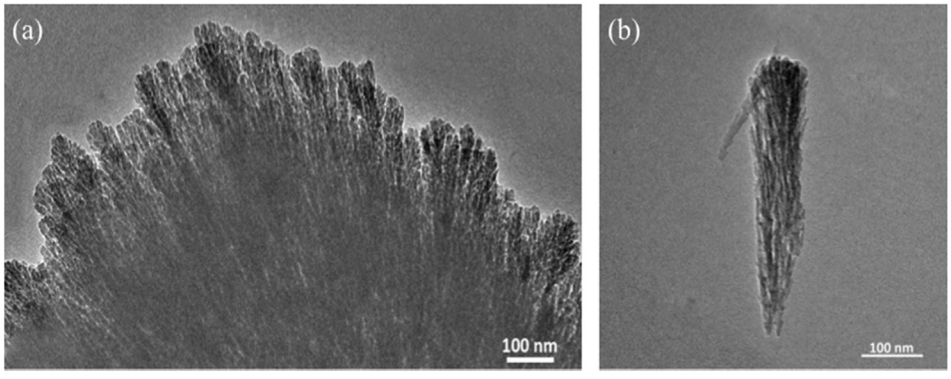

Fig. 3. HR-TEM images of (a) Si:H cauliflower-like structure and (b) an individual Si:H bundle.

Table 1
Summary of XRD data and calculated X_c values for the Si thin films deposited with different pressures.

Deposition pressure (mTorr)	2θ(degree)	FWHM(degree)	d_{XRD}(nm)	X_c(%)
10	28.46	0.84	9.7	49
15	28.42	1.07	7.6	23
25	28.42	1.57	5.2	15
35	–	–	–	–

X-ray diffraction (XRD) is another method to analyze the crystallization of thin films and evaluate their grain sizes. Fig. 4 shows the XRD spectra of the same samples. Although the RS spectra did not show any c-Si signal for films deposited at 35 mTorr (see Fig. 2(f)), the XRD spectra showed a broad peak with a shoulder located around 28.4°, which indicated the presence of crystallization in the (111) direction. This pattern indicated nanocrystal formation in the (111) direction towards the film surface; however, the film structure was still mostly composed of the amorphous phase owing to its wide full width at half maximum (FWHM) value. As the deposition pressure decreased, other crystal orientations could be seen clearly. At 25 mTorr, the Si (111) peak became more intense and two additional peaks attributed to (220) and (311) crystal orientations of Si were observed at 46.26^0 and 55.79^0, respectively. With a further decrease in the deposition pressure, the Si (400) and (331) crystal planes became slightly clear around 69^0 and 76^0, respectively. The intensity of the Si (111) peak increased more than the intensities of any other peaks with decreasing deposition pressure. Hence, the XRD spectrum indicated that preferential growth orientation of grains in the deposited films is towards the (111) crystal plane. According to Kakinuma et al., this preferential growth is explained by the lower surface energy of the (111) Si crystal orientation compared with the other crystal planes [46].

The average Si grain size can be estimated using the well-known Debye-Scherrer's formula:

$$d = \frac{k\lambda}{\beta \cos\theta} \tag{2}$$

where k is a shape factor, λ is the wavelength of X-ray radiation source, β is the FWHM of the signal at 28.4° diffraction angle, and θ is the Bragg angle.

The grain size of films estimated from the FWHM with diffraction angle of Si (111) signal using the Debye-Scherrer formula (Eqn. (2)) and calculated Raman crystallinity (Eqn. (1)) are summarized in Table 1. According to the XRD spectrum and Table 1, the grain size and crystallinity increased as the deposition pressure decreased. Additionally, the FWHM of the Si (111) signal decreased with the plasma pressure, which indicates higher crystallinity at lower plasma pressures. Based on both the RS and XRD results, it is clear that low deposition pressures favor volume crystalline fraction with larger grain sizes.

The crystallization dynamics of an ICP process are quite different than the dynamics of the conventional CCP process, in which the quality of crystallization degrades at low deposition pressures due to the lack of sufficient atomic H. This phenomenon results in insufficient H coverage of the film surface [47]. However, with ICP-CVD, the reactive H^* species and atomic hydrogen content in the plasma greatly increases due to excessive silane dissociation. The additional hydrogen may have a destructive etching effect on the Si network that provides disordered crystal lattices. Hence, over-abundant H-atoms cause degradation of the crystalline volume fraction [48].

3.4. Aging effect: oxidation of the film

FTIR measurements were conducted to determine the Si–H vibration modes and calculate the hydrogen content of the films. The FTIR absorption spectrum of Si thin films deposited with different deposition pressures is shown in Fig. 5 between 550 and 2200 cm^{-1}. Thin vertical dotted lines specify the position of the Si vibration modes. Absorption at 630 cm^{-1} was attributed to the Si–H rocking/wagging mode, the signal at 870 cm^{-1} was attributed to the Si–H_2 bending modes, remaining peak at ~2000–2030 cm^{-1} was ascribed to the Si-H_x ($1 \leq x \leq 3$) stretching modes and the Si–O–Si bridging mode at 1070–1080 cm^{-1}. The position of the wagging mode shifted slightly to lower frequencies with decreasing deposition pressure, as observed in the inset of Fig. 5. This shift has been reported to result from the rigid Si–Si bonds and increased crystallization at lower deposition pressures [45,49], which is consistent with the RS and XRD results presented in Section 3.3.

The most striking feature of the FTIR spectra was the presence of a strong Si–O–Si bridging mode signal between 1000 cm^{-1} and

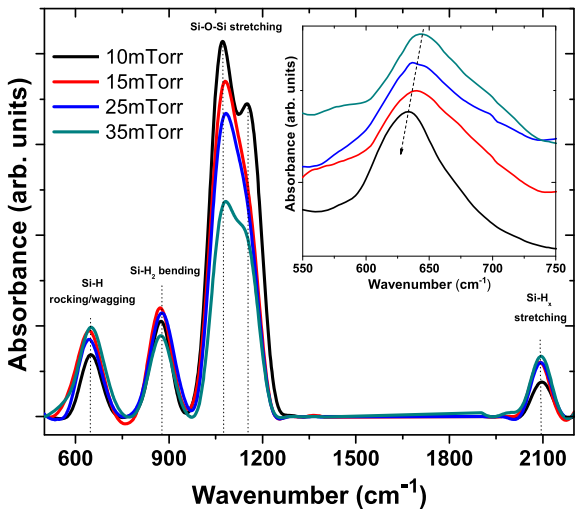

Fig. 5. FTIR spectra of the samples deposited with various deposition pressures. Inset, shifting of Si–H rocking/wagging mode with respect to deposition pressure is shown.

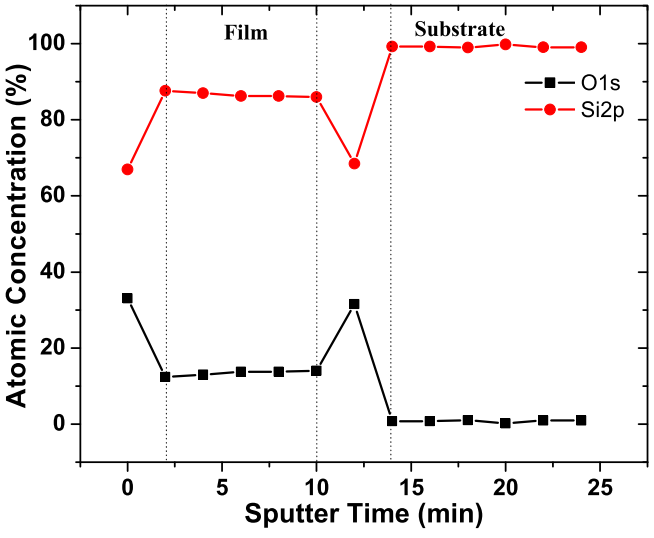

Fig. 6. Atomic concentration percentage of O and Si extracted from XPS depth-profiling analyses.

1200 cm^{-1}. To determine the variation of this stable oxide inside a film, we performed an XPS depth-profile analysis. Variation of the Si 2p and O 1s signals as a function of position from the film surface to substrate is displayed in Fig. 6 for the sample deposited at 25 mTorr. The oxygen content of the film was quite uniform, indicating that the film was uniformly oxidized. The uniform oxidation is related to the high porosity associated with the cauliflower-like structures that allows easy oxidation paths even at room temperature.

To understand the evolution of oxidation, the intensity of the oxidation concentration percentage was recorded as a function of time in a series of aging experiments. As seen in Fig. 7, no oxygen contamination was observed immediately after the deposition. However, the film oxidized drastically over time. The integrated area of the Si–O–Si bridging mode signal is displayed as a function of time in the inset of Fig. 7. We can see that the oxidation continues quite effectively even after 1 month.

It is possible to calculate the hydrogen concentrations of deposited films using signal intensities in the IR absorption spectrum. Since hydrogen content affects all optical and electrical properties of the films, it is very crucial to calculate the hydrogen content from the IR absorbance band. A commonly accepted method to determine the hydrogen concentration of films using the IR spectra is thoroughly explained in the studies of Mahan et al. and Kroll et al. [50,51].

The hydrogen content of the film was less than 6%. Low hydrogen content is a well-known feature of ICP-CVD-deposited thin films. In this study, thin film deposited at 35 mTorr had the lowest hydrogen content (C_H) (3.5%). Qin et al. [52] also reported a low C_H level of 3.8%; they suggested that the enhancement of hydrogen desorption may be responsible for the reduced hydrogen content Hydrogen has significant effect on light-induced degradation; experimental evidences revealed that hydrogen diffusion increases with illumination [6,53] and this light-induced hydrogen motion could enhance the light induced defect generation with breaking Si–Si bonds. Thus, low hydrogen content is quite essential for silicon layers used in solar cell applications.

4. Discussion

ICP-CVD offers high deposition rate and less ion bombardment on the surface of the substrate during the deposition. High deposition rate is highly desirable for the production of micro/nano crystalline layers for Si based thin film tandem structures. Low ion bombardment is an advantage in surface passivation of c-Si based solar cells. It was shown that Al_2O_3 deposition by ICP-CVD yielded a better passivation on the c-Si solar cells [54]. However, the film produced by ICP-CVD has peculiar properties that need to be addressed properly for its use in the active part of the device. The porous and cauliflower structure changing with time may not be good for stable electrical transport throughout the film. The electrical properties and their dependence on the film structure need to be carefully studied and clarified for an application to the device. On the other hand, the columnar film structure may however provide easy vertical carrier transport which is most essential for thin film devices. So, if the chemical instability like aging effect can be somehow eliminated, these films can be a good active absorber and charge carrier transport medium in solar cells. In addition, a-Si containing some oxygen will have a high optical band gap which is useful for window layer application. It was indeed shown that SiO_x is a good window material and provides improved internal refection [55]. Easy and vertical oxidation of the a-Si presented here can be further optimized to produce SiO_x material with desired optical and electrical properties for thin film solar cells. Another exciting possibility for these films is to use them in so-called third generation solar cells. The nanostructure nature of Si crystallites may lead to quantum confinement effect giving rise to production of tunable band gap material for all Si tandem solar cells. Finally, it is known that Si nanocrsytal and nanowires are promising alternative materials for lithium-ion battery applications due to smaller volume change of oxide during charge–discharge cycle than silicon itself [56,57]. Nanocrystalline Si thin film with high porosity fabricated by ICP-CVD may be a good alternative material for battery applications as well.

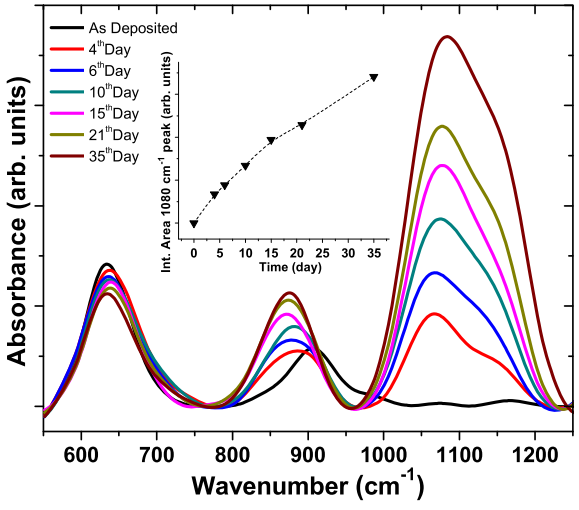

Fig. 7. Variation of FTIR spectra with time (inset) integrated area change of Si–O–Si stretching mode signal.

5. Conclusions

We investigated the structural and chemical properties of a-Si and nc-Si thin films prepared by ICP-CVD at room temperature with various deposition pressures. The crystallinity and deposition rate were strongly dependent on the pressure of the plasma generated by the inductively coupled plasma source. The Si grain size was also easily controlled through deposition pressure; however, the maximum grain size was only around 10 nm due to the low deposition temperature. Columnar growth and peculiar structures resembling cauliflower were observed in both a-Si and nc-Si thin films. The columnar and cauliflower-like structures were explained with two different approaches: one relates to the generated plasma species after the dissociation of silane and the other one is based on the well-known ballistic deposition theory. Since the depositions were performed at low temperature, the cold substrate restricts the lateral diffusion of the particles. This limitation is the origin of the columnar growth that promotes the development of the cauliflower-like structures. FTIR aging experiments indicated that the ICP-CVD-deposited Si structure is oxidized gradually and extremely uniform throughout the film when exposed to air due to its highly porous nature.

Acknowledgments

The author would like to acknowledge the CCR-Technology for manufacturing inductive source and VAKSIS-Company for incorporating a plasma thin film cluster tool. We thank Ilker Yıldız and Seckin Öztürk at METU Central Laboratory for XPS and TEM measurements, respectively.

References

[1] McEvoy A, Markvart T, Castaner L. Practical handbook of photovoltaics: fundamentals and applications: fundamentals and applications. Elsevier Science; 2003.

[2] Söderström K, Escarré J, Cubero O, Haug FJ, Perregaux S, Ballif C. Prog Photovolt Res Appl 2011;19:202–10.
[3] Strahm B, Howling A, Sansonnens L, Hollenstein C, Kroll U, Meier J, et al. Sol energy Mater Sol cells 2007;91:495–502.
[4] Bugnon G, Parascandolo G, Söderström T, Cuony P, Despeisse M, Hänni S, et al. Adv Funct Mater 2012;22:3665–71.
[5] Chen X, Jia B, Saha JK, Cai B, Stokes N, Qiao Q, et al. Nano Lett 2012;12:2187–92.
[6] Staebler DL, Wronski CR. Appl Phys Lett 1977;31:292.
[7] Green MA, Emery K, Hishikawa Y, Warta W, Dunlop ED. Prog Photovolt Res Appl 2013;21:1–11.
[8] Parashar A, Kumar S, Dixit PN, Gope J, Rauthan CMS, Hashmi SA. Sol Energy Mater Sol Cells 2008;92:1199–204.
[9] Mai Y, Klein S, Carius R, Wolff J, Lambertz A, Finger F, et al. J Appl Phys 2005;97:114913.
[10] Cheng Q, Xu S, Huang S, Ostrikov K. Cryst Growth Des 2009;9:2863–7.
[11] Sriraman S, Agarwal S, Aydil ES, Maroudas D. Nature 2002;418:62–5.
[12] Dalal VL, Graves J, Leib J. Appl Phys Lett 2004;85:1413.
[13] Kim SÄ, Han SÄ, Kuk SÄ, Kang DÄ, Ha TÄ, Han MÄ. Nanocrystalline silicon thin film transistor fabricated without any substrate heating for a flexible display. In: SID symposium digest of technical papers. Wiley Online Library; 2008. p. 1262–5.
[14] Ostrikov KN, Xu S, Yu MY. J Appl Phys 2000;88:2268.
[15] Dao VA, Duy NV, Heo J, Choi H, Kim Y, Yi J. Jpn J Appl Phys 2009;48:6509.
[16] Zhou HP, Wei DY, Xu S, Xiao SQ, Xu LX, Huang SY, et al. J Appl Phys 2012;112:013708.
[17] Xiao SQ, Xu S, Zhou HP, Wei DY, Huang SY, Xu LX, et al. Appl Phys Lett 2012;100:233902.
[18] Zhou HP, Wei DY, Xu LX, Guo YN, Xiao SQ, Huang SY, et al. Appl Surf Sci 2013;264:21–6.
[19] Dergez D, Schalko J, Bittner A, Schmid U. Appl Surf Sci 2013;284:348–53.
[20] Shen C-H, Shieh J-M, Huang JY, Kuo H-C, Hsu C-W, Dai B-T, et al. Appl Phys Lett 2011;99:033510.
[21] Mavilla NR, Rai DKR, Solanki CS, Vasi J. Optical bandgap tuning of ICPCVD-made silicon nanocrystals for next generation photovoltaics. In: Photovoltaic specialists conference (PVSC), 2012 38th IEEE; 2012. p. 000806–9.
[22] Shen Z, Kim T, Kortshagen U, McMurry PH, Campbell SA. J Appl Phys 2003;94:2277.
[23] Cheng Q, Xu S, Ostrikov K. Nanotechnology 2009;20:215606.
[24] Barabasi AL, Stanley HE. Fractal concepts in surface growth. Cambridge: Cambridge university press; 1995.
[25] Mani RC, Pavel I, Aydil ES. J Appl Phys 2007;102:043305.
[26] Tochikubo F, Suzuki A, Kakuta S, Terazono Y, Makabe T. J Appl Phys 1990;68:5532.
[27] Rech B, Repmann T, Wieder S, Ruske M, Stephan U. Thin Solid Films 2006;502:300–5.
[28] Takatsuka H, Noda M, Yonekura Y, Takeuchi Y, Yamauchi Y. Sol Energy 2004;77:951–60.
[29] Howling AA, Strahm B, Hollenstein C. Thin Solid Films 2009;517:6218–24.
[30] Herman IP. Optical diagnostics for thin film processing. Academic Press; 1996.
[31] Matsuda A. Jpn J Appl Phys 2004;43:7909–20.
[32] Nomoto K, Urano Y, Guizot JL, Ganguly G, Matsuda A. Jpn J Appl Phys 1990:1372.
[33] Tsai CC, Knights JC, Chang G, Wacker B. J Appl Phys 1986;59:2998.
[34] Kovalgin AY, Boogaard A, Brunets I, Holleman J, Schmitz J. Surf Coatings Technol 2007;201:8849–53.
[35] Robledo A, Grabill CN, Kuebler SM, Dutta A, Heinrich H, Bhattacharya A. Phys Rev E 2011;83.
[36] Krug J, Meakin P. Phys Rev A 1991;43:900–19.
[37] Saito Y, Omura S. Phys Rev E 2011;84.
[38] Gorsky A, Nechaev S, Santachiara R, Schehr G. Nucl Phys B 2012;862:167–92.
[39] Šmíd B, Li Z, Dohnálková A, Arey BW, Smith RS, Matolín V, et al. J Phys Chem C 2012;116:10649–55.
[40] Flaherty DW, Dohnalek Z, Dohnalkova A, Arey BW, McCready DE, Ponnusamy N, et al. J Phys Chem C 2007;111:4765–73.
[41] Dohnalek Z, Kimmel GA, McCready DE, Young JS, Dohnalkova A, Smith RS, et al. J Phys Chem B 2002;106:3526–9.
[42] Mukhopadhyay S, Das C, Ray S. J Phys D: Appl Phys 2004;37:1736–41.
[43] Shah A. Thin-film silicon solar cells. Lausanne: Epfl Press; 2010.
[44] Song D, Cho E-C, Conibeer G, Flynn C, Huang Y, Green MA. Sol Energy Mater Sol Cells 2008;92:474–81.
[45] Han D, Wang K, Owens JM, Gedvilas L, Nelson B, Habuchi H, et al. J Appl Phys 2003;93:3776.
[46] Kakinuma H, Mohri M, Sakamoto M, Tsuruoka T. J Appl Phys 1991;70:7374.
[47] Matsuda A. Thin Solid Films 1999;337:1–6.
[48] Li J, Wang J, Yin M, Gao P, He D, Chen Q, et al. J Appl Phys 2008;103:043505.
[49] Adachi MM, Kavanagh KL, Karim KS. J Vac Sci Technol A Vac Surf Films 2007;25:464.
[50] Mahan AH, Gedvilas LM, Webb JD. J Appl Phys 2000;87:1650.
[51] Kroll U, Meier J, Shah A, Mikhailov S, Weber J. J Appl Phys 1996;80:4971.
[52] Qin Y, Yan H, Li F, Qiao L, Liu Q, He D. Appl Surf Sci 2010;257:817–22.
[53] Santos P, Johnson N, Street R. Phys Rev Lett 1991;67:2686–9.
[54] Veith B, Dullweber T, Siebert M, Kranz C, Werner F, Harder N-P, et al. Energy Procedia 2012;27:379–84.
[55] Cuony P, Alexander DTL, Perez-Wurfl I, Despeisse M, Bugnon G, Boccard M, et al. Adv Mater 2012;24(9):1182–6.
[56] Mamiya M, Takei H, Kikuchi M, Uyeda C. J Cryst growth 2001;229:457–61.
[57] Kulish VV, Malyi OI, Ng M-F, Wu P, Chen Z. Rsc Adv 2013;3:4231–6.